

REPORT DOCUMENTATION PAGE					Form Approved OMB No. 0704-0188	
<p>The public reporting burden for this collection of information is estimated to average 1 hour per response, including the time for reviewing instructions, searching existing data sources, gathering and maintaining the data needed, and completing and reviewing the collection of information. Send comments regarding this burden estimate or any other aspect of this collection of information, including suggestions for reducing the burden, to the Department of Defense, Executive Service Directorate (0704-0188). Respondents should be aware that notwithstanding any other provision of law, no person shall be subject to any penalty for failing to comply with a collection of information if it does not display a currently valid OMB control number.</p> <p>PLEASE DO NOT RETURN YOUR FORM TO THE ABOVE ORGANIZATION.</p>						
1. REPORT DATE (DD-MM-YYYY) 02-23-2011		2. REPORT TYPE Final Technical Report			3. DATES COVERED (From - To) 01/01/2008-11/30/2010	
4. TITLE AND SUBTITLE Implicit LES for Supersonic Microramp Vortex Generator - New Discoveries and New Mechanisms					5a. CONTRACT NUMBER	
					5b. GRANT NUMBER FA9550-08-1-0201	
					5c. PROGRAM ELEMENT NUMBER	
					5d. PROJECT NUMBER	
6. AUTHOR(S) Chaoqun Liu and Frank Lu					5e. TASK NUMBER	
					5f. WORK UNIT NUMBER	
7. PERFORMING ORGANIZATION NAME(S) AND ADDRESS(ES) University of Texas at Arlington Department of mathematics 411 S. Nedderman, 4th floor Arlington, TX 76019					8. PERFORMING ORGANIZATION REPORT NUMBER	
9. SPONSORING/MONITORING AGENCY NAME(S) AND ADDRESS(ES) John D. Schmisser, Ph.D. Air Force Office of Scientific Research ATTN: John Schmisser -NA 875 North Randolph Street Suite 325, Room 3112					10. SPONSOR/MONITOR'S ACRONYM(S) AFOSR	
					11. SPONSOR/MONITOR'S REPORT NUMBER(S) AFRL-OSR-VA-TR-2012-0901	
12. DISTRIBUTION/AVAILABILITY STATEMENT Unlimited distribution Distribution A: Approved for Public Release						
13. SUPPLEMENTARY NOTES						
14. ABSTRACT This final technical report serves as a summary of our recent work on LES and experiments on supersonic MVG. An implicitly implemented large eddy simulation (ILES) by using the fifth order WENO scheme is applied to study the flow around the microramp vortex generator (MVG) at Mach 2.5. A number of new discoveries on the flow around supersonic MVG has been made including spiral points, surface separation topology, source of the momentum deficit, inflection surface, Kelvin-Helmholtz instability, vortex ring generation, ring-shock interaction, 3-D recompression shock structure, influence of MVG decline angles. Most of the new discoveries, which were made in 2009, were confirmed by experiments conducted by the UTA experimental team in 2010. A new 5-pair-vortex-tube model near the MVG is given based on the ILES observation. The vortex ring-shock interaction is found as the new mechanism of the reduction of the separation zone induced by the shock-boundary layer interaction.						
15. SUBJECT TERMS						
16. SECURITY CLASSIFICATION OF:			17. LIMITATION OF ABSTRACT	18. NUMBER OF PAGES	19a. NAME OF RESPONSIBLE PERSON Chaoqun Liu	
a. REPORT Public	b. ABSTRACT Public	c. THIS PAGE Public			19b. TELEPHONE NUMBER (Include area code) 817-272-5151	

Implicit LES for Supersonic Microramp Vortex Generator - New Discoveries and New Mechanisms

(Final Technical Report for AFOSR Grant No. FA9550-08-1-0201)

Chaoqun Liu and Frank Lu
University of Texas at Arlington, Arlington, Texas, 76019
cliu@uta.edu

February 2011

This final technical report serves as a summary of our recent work on LES and experiments on supersonic MVG. An implicitly implemented large eddy simulation (ILES) by using the fifth order *WENO* scheme is applied to study the flow around the microramp vortex generator (MVG) at Mach 2.5. A number of new discoveries on the flow around supersonic MVG has been made including spiral points, surface separation topology, source of the momentum deficit, inflection surface, Kelvin-Helmholtz instability, vortex ring generation, ring-shock interaction, 3-D recompression shock structure, influence of MVG decline angles. Most of the new discoveries, which were made in 2009, were confirmed by experiments conducted by the UTA experimental team in 2010. A new 5-pair-vortex-tube model near the MVG is given based on the ILES observation. The vortex ring-shock interaction is found as the new mechanism of the reduction of the separation zone induced by the shock-boundary layer interaction.

Key Words: Micro vortex generator, shock-boundary layer interaction, vortex ring, shock-ring interaction

Nomenclature

M	=	Mach number
Re_θ	=	Reynolds number based on momentum thickness
c	=	micro ramp vortex generator side length
h	=	MVG height
α	=	MVG half angle
β	=	MVG declining angle of the trailing edge
δ	=	incompressible boundary-layer nominal thickness
δ^*	=	incompressible boundary-layer displacement thickness
θ	=	incompressible boundary-layer momentum thickness
H_i	=	incompressible boundary-layer shape factor δ^*/θ
x, y, z	=	spanwise, normal and streamwise coordinate axes
u, v, w	=	spanwise, normal and streamwise velocities

p_0	= Pitot pressure
$C_{P_{tot_{rc}}}$	= Pitot pressure recovery coefficient
Pr	= Prandtl number
RANS	= Reynolds-averaged Navier-Stokes
LES	= large eddy simulation
DNS	= direct numerical simulation
WENO	= weighted essentially non-oscillatory scheme
TVB	= total variation bounded
SBLI	= shock wave boundary layer interaction
VG	= vortex generator
MVG	= microramp VG
Subscript	
w	= wall
∞	= free stream
0	= representing the location at the inlet if without special explanation

I. Introduction

It is well known that for supersonic flow past a ramp, shock boundary layer interaction (SBLI) can significantly degrade the quality of the flow field by triggering large-scale separation, causing total pressure loss, making the flow unsteady and distorted, and can even make an engine unable to start. In order to improve the “health” of the boundary layer, a series of new devices known as micro vortex generators, with a height approximately 20-40% of the boundary layer thickness, is suggested for flow control. Specifically, because of its robust structure, the microramp vortex generator (MVG) is attractive to the inlet designer. Intensive computational and experimental studies have been made on the MVG recently.

Lin indicated (2002) that a device such as an MVG can alleviate the flow distortion in compact ducts to some extent and control boundary layer separation due to adverse pressure gradients. Similar comments were made in the review by Ashill et al (2005). Systematic studies on micro VGs including micro ramp VGs in supersonic flow can be found in the paper by Anderson et al. (2006). Babinsky (2009) performed a series of experiments on different kinds of micro VGs and investigated their control effects in detail. The mechanism of MVG flow control from his work was described as a pair of counter-rotating primary streamwise vortices generated by the MVG, which is mainly located within the boundary layer and travels downstream for a considerable distance. Secondary vortices are located underneath the primary ones and even more streamwise vortices could be generated under suitable conditions. Streamwise vortices inside the boundary later bring low momentum fluid up from the bottom and high momentum fluid down to the boundary layer. A striking circular momentum deficit region is observed in the wake behind the MVG. The vortices lift up slowly, which is thought to be the consequence of the upwash effect of the vortices.

Numerical simulations have been made on MVG for comparative study and further design purposes. Ghosh, Choi and Edwards (2010) made detailed computations under the experimental conditions given by Babinsky by using RANS, hybrid RANS/LES and immersed boundary (IB) techniques. Lee et al (2009, 2010) also made computations on MVGs problems by using Monotone Integrated Large Eddy Simulations (MILES). Basic flow

structures like momentum deficit and streamwise vortices were reproduced in the computation. Further studies were also conducted on the improvement of the control effect.

The actual physical mechanisms of how MVGs control the flow are definitely needed for design purposes. RANS, DES, RANS/DES, RANS/LES, etc are good engineering tools, but may not be able to reveal the mechanism and obtain deep understanding of MVG. We need high-order DNS/LES. A powerful approach is the integration of high order LES and experiment. Recently, an implicit LES for MVG to control the shock-boundary layer interaction around a 24 degree ramp at Mach number of 2.5 and Reynolds number of 1440 has been carried out (Li & Liu, January 2010). In this work, several new discoveries have been made and the mechanism of MVG is found to be quite different from those reported by previous experimental and numerical work. The new findings include: 1) Spiral points and flow topology around MVG; 2) New theory of five pairs of vortices near MVG; 3) Origin of momentum deficit; 4) Inflection points (surface for 3-D) and Kelvin-Helmholtz (K-H) type instability; 5) Vortex ring generation; 6) Ring-shock interaction and separation reduction; 7) 3-D re-compressed shock structure; 8) Effects of MVG trailing-edge angles.

Most of the new discoveries were made by October 2009 and were later confirmed by the UTA experimental work in April 2010 (Lu et al., 2010). Based on our observations, the mechanism of MVG to reduce the flow separation is really caused by interaction of shock and vortex rings generated by MVG.

II. Numerical Methods

2.1 Governing equations

The governing equations are the non-dimensional Navier-Stokes equations in conservative form as follows:

$$\frac{\partial Q}{\partial t} + \frac{\partial E}{\partial x} + \frac{\partial F}{\partial y} + \frac{\partial G}{\partial z} = \frac{\partial E_v}{\partial x} + \frac{\partial F_v}{\partial y} + \frac{\partial G_v}{\partial z}, \quad (1)$$

where

$$Q = \begin{bmatrix} \rho \\ \rho u \\ \rho v \\ \rho w \\ e \end{bmatrix} \quad E = \begin{bmatrix} \rho u \\ \rho u^2 + p \\ \rho uv \\ \rho uw \\ (e + p)u \end{bmatrix} \quad F = \begin{bmatrix} \rho v \\ \rho vu \\ \rho v^2 + p \\ \rho vw \\ (e + p)v \end{bmatrix} \quad G = \begin{bmatrix} \rho w \\ \rho wu \\ \rho wv \\ \rho w^2 + p \\ (e + p)w \end{bmatrix}$$

$$E_v = \frac{1}{\text{Re}} \begin{bmatrix} 0 \\ \tau_{xx} \\ \tau_{xy} \\ \tau_{xz} \\ u\tau_{xx} + v\tau_{xy} + w\tau_{xz} + q_x \end{bmatrix} \quad F_v = \frac{1}{\text{Re}} \begin{bmatrix} 0 \\ \tau_{yx} \\ \tau_{yy} \\ \tau_{yz} \\ u\tau_{yx} + v\tau_{yy} + w\tau_{yz} + q_y \end{bmatrix} \quad G_v = \frac{1}{\text{Re}} \begin{bmatrix} 0 \\ \tau_{zx} \\ \tau_{zy} \\ \tau_{zz} \\ u\tau_{zx} + v\tau_{zy} + w\tau_{zz} + q_z \end{bmatrix}$$

$$e = \frac{p}{\gamma - 1} + \frac{1}{2} \rho(u^2 + v^2 + w^2) \quad q_x = \frac{\mu}{(\gamma - 1)M_\infty^2 \text{Pr}} \frac{\partial T}{\partial x} \quad q_y = \frac{\mu}{(\gamma - 1)M_\infty^2 \text{Pr}} \frac{\partial T}{\partial y}$$

$$q_z = \frac{\mu}{(\gamma - 1)M_\infty^2 \text{Pr}} \frac{\partial T}{\partial z} \quad p = \frac{1}{\gamma M_\infty^2} \rho T \quad \text{Pr} = 0.72$$

$$\tau = \mu \begin{bmatrix} \frac{4}{3} \frac{\partial u}{\partial x} - \frac{2}{3} (\frac{\partial v}{\partial y} + \frac{\partial w}{\partial z}) & \frac{\partial u}{\partial y} + \frac{\partial v}{\partial x} & \frac{\partial u}{\partial z} + \frac{\partial w}{\partial x} \\ \frac{\partial u}{\partial y} + \frac{\partial v}{\partial x} & \frac{4}{3} \frac{\partial v}{\partial y} - \frac{2}{3} (\frac{\partial w}{\partial z} + \frac{\partial u}{\partial x}) & \frac{\partial v}{\partial z} + \frac{\partial w}{\partial y} \\ \frac{\partial u}{\partial z} + \frac{\partial w}{\partial x} & \frac{\partial v}{\partial z} + \frac{\partial w}{\partial y} & \frac{4}{3} \frac{\partial w}{\partial z} - \frac{2}{3} (\frac{\partial u}{\partial x} + \frac{\partial v}{\partial y}) \end{bmatrix}$$

The viscous coefficient is given by Sutherland's equation:

$$\mu = T^{\frac{3}{2}} \frac{1+C}{T+C}, \quad C = \frac{110.4}{T_{\infty}} \quad (2)$$

The non-dimensional variables are defined as follows:

$$x = \frac{\tilde{x}}{L}, y = \frac{\tilde{y}}{L}, z = \frac{\tilde{z}}{L}, u = \frac{\tilde{u}}{U_{\infty}}, v = \frac{\tilde{v}}{U_{\infty}}, w = \frac{\tilde{w}}{U_{\infty}},$$

$$T = \frac{\tilde{T}}{T_{\infty}}, \mu = \frac{\tilde{\mu}}{\mu_{\infty}}, k = \frac{\tilde{k}}{k_{\infty}}, \rho = \frac{\tilde{\rho}}{\rho_{\infty}}, p = \frac{\tilde{p}}{\rho_{\infty} U_{\infty}^2}, e = \frac{\tilde{e}}{\rho_{\infty} U_{\infty}^2},$$

where the variables with '~' are the dimensional counterparts.

Considering the following grid transformation,

$$\begin{cases} \xi = \xi(x, y, z) \\ \eta = \eta(x, y, z) \\ \zeta = \zeta(x, y, z) \end{cases} \quad (3)$$

the Navier-Stokes equations can be transformed to the system using generalized coordinates:

$$\frac{\partial \hat{Q}}{\partial \tau} + \frac{\partial \hat{E}}{\partial \xi} + \frac{\partial \hat{F}}{\partial \eta} + \frac{\partial \hat{G}}{\partial \zeta} = \frac{\partial \hat{E}_v}{\partial \xi} + \frac{\partial \hat{F}_v}{\partial \eta} + \frac{\partial \hat{G}_v}{\partial \zeta} \quad (4)$$

where $\hat{Q} = J^{-1}Q$ and

$$\hat{E} = J^{-1}(\xi_x E + \xi_y F + \xi_z G), \quad \hat{F} = J^{-1}(\eta_x E + \eta_y F + \eta_z G), \quad \hat{G} = J^{-1}(\zeta_x E + \zeta_y F + \zeta_z G)$$

$$\hat{E}_v = J^{-1}(\xi_x E_v + \xi_y F_v + \xi_z G_v), \quad \hat{F}_v = J^{-1}(\eta_x E_v + \eta_y F_v + \eta_z G_v), \quad \hat{G}_v = J^{-1}(\zeta_x E_v + \zeta_y F_v + \zeta_z G_v),$$

J^{-1}, ξ_x , etc are grid metrics, and $J^{-1} = \det\left(\frac{\partial(x, y, z)}{\partial(\xi, \eta, \zeta)}\right), \xi_x = J(y_\eta z_\zeta - z_\eta y_\zeta)$, etc.

2.2 Finite difference schemes and boundary conditions

1. The 5th order WENO scheme for the convective terms (Jiang & Shu, 1996)

In order to decrease the dissipation of the scheme, the less dissipative Steger-Warming flux splitting method is used in the computation, but not the commonly-used dissipative Lax-Friedrich splitting method.

2. The difference scheme for the viscous terms

Considering the conservative form of the governing equations, the traditional 4th order central scheme is used twice to compute the 2nd order derivatives for viscous terms.

3. The time scheme

The basic methodology for the temporal terms in the Navier-Stokes equations adopts the explicit 3rd order TVD-type Runge-Kutta scheme:

$$\begin{aligned} u^{(1)} &= u^n + \Delta t L(u^n) \\ u^{(2)} &= \frac{3}{4}u^n + \frac{1}{4}u^{(1)} + \frac{1}{4}\Delta t L(u^{(1)}) \\ u^{n+1} &= \frac{1}{3}u^n + \frac{2}{3}u^{(2)} + \frac{2}{3}\Delta t L(u^{(2)}) \end{aligned} \quad (5)$$

4. Boundary conditions

The adiabatic, zero-gradient of pressure and non-slipping conditions are used for the wall as:

$$\partial T / \partial n = 0, \partial p / \partial n = 0, \vec{U} = 0 \quad (6)$$

To enforce the free stream condition, fixed value boundary condition with the free parameters is used on the upper boundary. The boundary conditions at the front and back boundary surface in the spanwise direction are given as the mirror-symmetry condition. The outflow boundary conditions are specified as a kind of characteristic-based condition, which can handle the outgoing flow without reflection.

The inflow conditions are generated using the following steps:

a) A turbulent mean profile is obtained from DNS by Liu & Chen (2010) for the streamwise velocity (w -velocity) and the distribution is scaled using the local displacement thickness and free stream velocity.

b) Random fluctuations are added on the primitive variables, i.e. u, v, w, p, ρ . The disturbance has the form: $\epsilon_{distb} e^{-(y-y_w)^2 / \Delta y_{distb}} \times (random - 0.5) / 2$, where the subscript ‘distb’ means the disturbance, “random” is the random function with the value between 0~1, ϵ_{distb} equals to 0.1 and Δy_{distb} equals to $2/3\delta_0$.

Such inflow conditions are, of course, not the fully developed turbulent flow, but we can consider it as a weakly disturbed inflow while propagating downstream.

5. Body-fitted grid generation

The geometry of MVG is shown in Fig. 1. In order to alleviate the difficulty to grid generation caused by original vertical trailing-edge, a modification is made by declining the edge to 70°. The other geometric parameters in the figure are the same as those given by Babinsky (2007), i.e., $c=7.2h$, $\alpha=24^\circ$ and $s=7.5h$, where h is the height of MVG and s is the distance between the center lines of two adjacent MVGs. So the distance from the center line to the spanwise boundary of the computation domain is $3.75h$.

According to experiments by Babinsky (2007), the ratio h/δ_0 of the models has the range from 0.3~1. The appropriate distance from the trailing-edge to the control area is around $19\sim 56h$ or $8\sim 19\delta_0$. So in this study, the height of MVG h is assumed to be $\delta_0/2$ and the horizontal distance from the apex of MVG to the ramp corner is set to be $19.5h$ or $9.75\delta_0$. The distance from the end of the ramp to the apex is $32.2896h$. The distance from the starting point of the domain to the apex of MVG is $17.7775h$. The height of the domain is from $10h$ to $15h$ and the width of the half domain is $3.75h$. The geometric relation of the half of the domain can be seen in Fig. 2, where the symmetric plane is the centre plane.

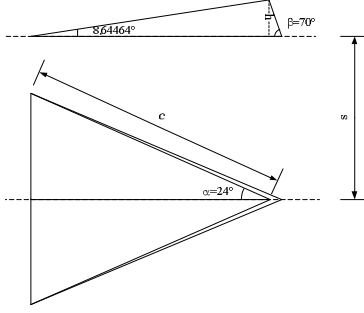


Figure 1. The geometry of MVG

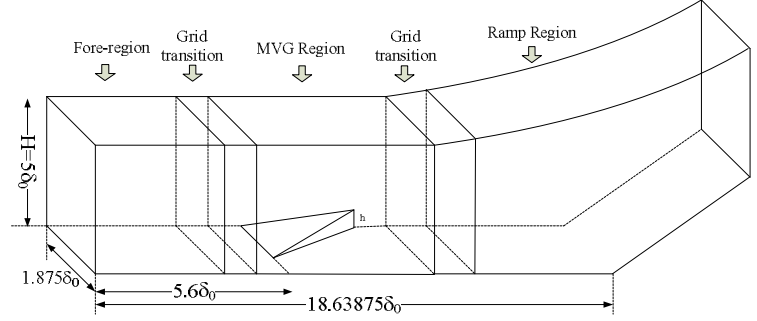
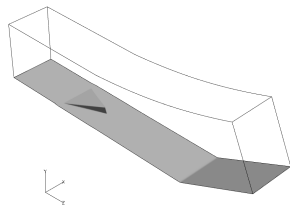
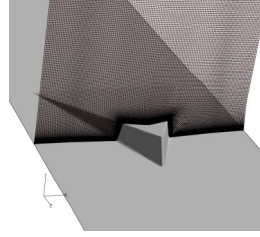


Figure 2. The schematic of the half grid system of case 1

The grid number for the whole system is: $n_{spanwise} \times n_{normal} \times n_{streamwise} = 128 \times 192 \times 1600$. We try to make the grids smooth and orthogonal as much as possible (Fig. 3).

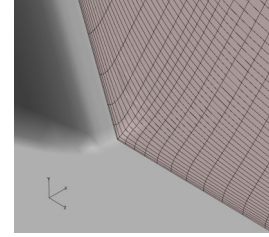


(a) domain



Computational

(b) The grid section intersecting the middle of MVG



(c) The grids at the corner of MVG

Figure 3. Body-fitted grid system

2.3 Code validation

1. Supersonic ramp

Figure 4 gives the instantaneous numerical schlieren image of the central plane, which uses the value of $|\nabla \rho|$. For qualitative comparison, an experimental picture of ramp flow at $M=2.9$ with large Reynolds number is given in Fig. 5 obtained from the experiment by Loginov et al (2006). From both pictures, we can observe that the separation shock wave has an angle which is a little larger but nearly the same to the ramp angle and is almost aligned with the reflection shock (which is more obvious in the experimental result).



Figure 4. The digital schlieren at central plane

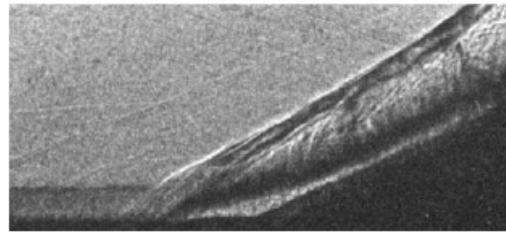


Figure 5. The experimental schlieren by Loginov et al (2006)

2. Supersonic MVG

Babinsky (2009) presented the structure of the wave system, i.e., the first reflection shock, the expansion wave system and the re-compression shock, as shown in Fig. 6. The first shock will turn within the incoming boundary layer due to “the change in Mach number”, and “a second shock wave then turns the flow back to horizontal”. A subtle oblique “ λ ” structure is observed at the foot of the re-compression shock. The numerical schlieren picture of the time-averaged flow field at the central plane is presented in Fig. 7. From the figure, the two shock waves are

well described by the computation. The turning of the main shock to the wall can be distinguished; the oblique “ λ ” structure can be found on the foot of the second shock as well. Table 1 gives a comparison between numerical and experimental results. The measured shock angles from Babinsky’s experiment are: 26.869° for the first shock, and 21.93° for the re-compression shock. In contrast, the computational values are: 26.988° for the first shock, and 24.656° for the re-compression shock. Considering the declining angle of the trailing-edge is 70° , not the 90° as in the experiment, the computational results show a reasonable agreement with experiment and of a high degree of resolution.

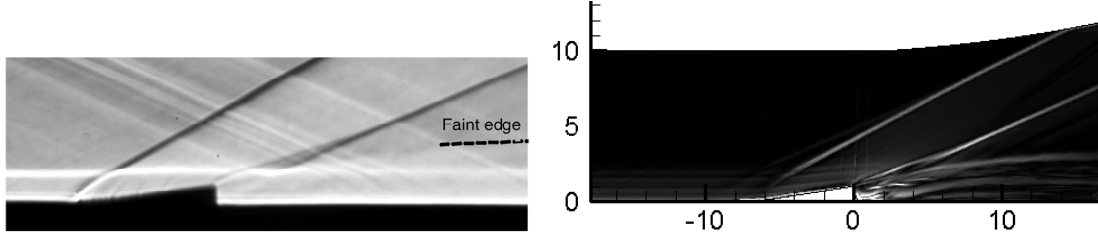


Figure 6. The experimental schlieren by Babinsky (2009) Figure 7. The numerical schlieren at central plane

Table 1 Comparison between IIES and experiment in shock angles

	1st shock	2nd shock
Experiment	26.869°	21.93°
Computation	26.988°	24.656°

III. Experimental Methods

3.1 Test facility

The experiments were performed in a blowdown wind tunnel. The tunnel has a continuously variable Mach number range of 1.5–4 and a Reynolds number range of 60–140 million/m. The total air storage was 24.5 m^3 (865 ft^3) at 5.3 MPa (750 psig) which allowed for runs of as long as 90 s. For this series of experiments, the Mach number was fixed nominally at 2.45 by removing the variable Mach number feature and installing fix adaptor plates between the nozzle and the test section.

The test section is $15.2 \text{ cm}^2 \times 81.28 \text{ cm}$ long ($6 \text{ in.}^2 \times 2.67 \text{ ft}$). It was outfitted with extensive optical access from both sides and from the top. Figure 8 is a CAD mockup showing a configuration with transparencies in the front half only.

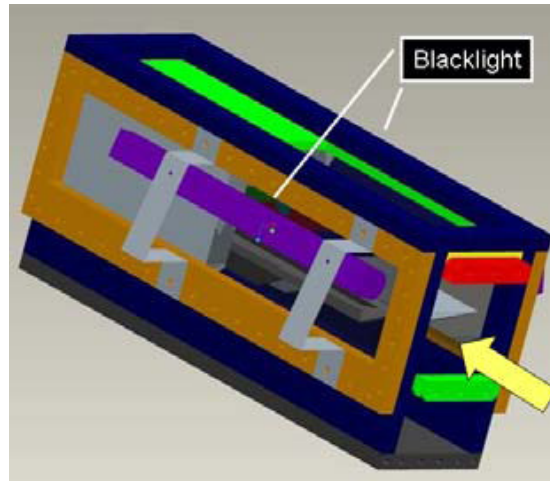


Figure 8. CAD mockup showing half transparency on the ceiling and sides. Flow from right to left.

3.2 Test model

A boundary layer was developed naturally over a flat plate with a sharp leading edge of 15 deg. The plate spanned the test section and was 73 cm (28.75 in.) long. The flat plate was made in layers supported by a sharp-tipped rail on each side. The top layer which was the test surface was made of a number of small, thin plates (Fig. 9). These plates butted tightly against each other to form a continuous, flat surface. This modular design allows for quick configuration changes. A cavity existed below the top surface for allowing pressure tubing, transducer wiring and other elements to be fitted. The wiring and tubing were channeled to the rear to the diffuser and outside of the flat plate in a pipe. A bottom surface encased the cavity.



Figure 9. Test section showing flat plate. Flow from right to left.

Other than the flat plate itself, for the present study, various shock generators could be placed at 32.4 cm (12.75 in.) from the leading edge. These shock generators included a 5 or a 16 deg compression ramp and a 12.7 mm (0.5 in.) diameter upright cylinder.

A micro-vortex generator (MVG) array was mounted ahead of the ramp. Based on the recommendations of Anderson et al. (2006), for the present experiments where the boundary layer was about 3–4 mm thick, the array was mounted 5.2 mm (0.205 in.) ahead of the ramp. Figure 10 shows an array of five MVGs. Each MVG was 12.95 mm (0.51 in.) long and 1.57 mm (0.062 in.) high. The front of the MVG was 11.7 mm (0.46 in.) wide. The center-to-center spacing between the MVGs was 30.5 mm (1.2 in.). Two styles of MVGs were fabricated based on the designs from Li and Liu (2010), based on the trailing edge angle of 45 or 70 deg.



Figure 10. Micro-vortex generator array.

3.3 Test conditions

Wind tunnel conditions were monitored by a total pressure and a total temperature probe in the plenum chamber and by a static orifice near the exit of the nozzle. The test Mach number is 2.47 ± 0.005 . The total pressure is maintained at 551 ± 6 kPa (80 ± 0.9 psia). The tunnel operation is controlled by a host computer which opened the control valve to reach steady-state conditions in about 2–3 s. The blowdown operation caused the total temperature to drop by 5 K in 30 s. Since the duration of the flow visualization experiments were less than 10 s long, the temperature drop was not significant. Thus, the unit Reynolds number can be considered to be steady at 43 million per m.

3.4 Surface flow visualization

The surface flow visualization technique consisted of painting bands of fluorescent mixture along the surface of the plate ahead of the area of interest. (The use of fluorescent pigments with ultraviolet light in producing bright

images has been reported previously, including for determining skin friction. Based on previous experience, a kerosene carrier evaporates readily in such test conditions to leave a dry trace within 10 s. For the present experiments, a mixture of kerosene and fluorescent chalk with a small quantity of silicone oil was found to be suitable. The exact composition required some trial and error but, generally, the mixture should have a consistency of syrup. The particle size of the ground chalk was reduced to 100 μm by straining the mixture. The small particle size improved the resolution of fine features.

A Canon Vixia HF S10 high-definition camcorder was placed perpendicularly overhead to acquire the images. This camcorder has a 2.39 megapixel (1.56 effective megapixels for video) HD CMOS sensor and frame rates of 24 or 30 per s. The maximum shutter speed, as used in the present recordings, is 1/2000 s. A still camera (Nikon D300S with a VR 18–200 mm F/3.5-5.6 lens and operated typically 1/8000 s shutter speed) was also available and can be mounted side-by-side with the video camera. The Nikon camera has a 13.1 megapixel (12.3 effective megapixel) CMOS image sensor and can capture high-definition video at 24 fps. It can be noted that the Nikon camera produces very high-resolution images that are useful for resolving small features.

“Black light” tubes (Utilitech Model Gu9721P-T8-BKI) placed on both sides of the test section were used to illuminate the mixture without turning off the ambient fluorescent lighting (Fig. 8). Figure 11 shows the bands of fluorescent mixture under black light that were applied ahead of the MVG array. Three of the MVGs that within the picture are highlighted by dashed lines. The extensive optical access in the present facility allowed the cameras to be placed perpendicularly to the test surface. This helps to minimize geometric errors. Finally, the digital processing was applied to the still or video images.

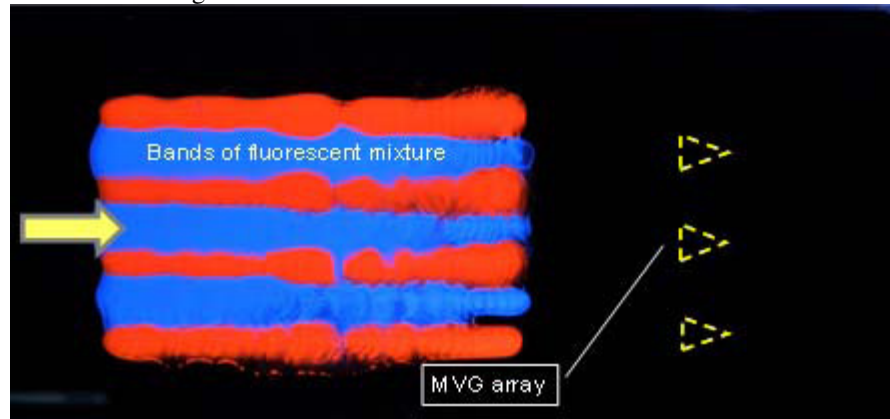


Figure 11. Bands of fluorescent mixture applied to test surface.

The emphasis here is to process video images to highlight small, obscure features. Following a review of a videoclip, the interesting segment was decompiled into individual frames using Blaze Media ProTM. The individual frames were imported into DaVisTM 7.1 which is software from LaVision for processing particle image velocimetry images.

Two nonlinear filters were used to highlight the small, obscure features. The first nonlinear filter is known as the “non-linear concentration” filter. As the paint thinned over the surface, a smoothing effect was noticed over a large range of pixels. The “non-linear concentration” filter searches for the local maximum intensity which is above a user-defined pixel noise level (set to 10 for the present purpose), and concentrates the local maximum to the center of a defined pixel area which is typically taken to be a 7×7 pixel area. The result of this operation is to convert the color image into a high-contrast gray scale image. The second non-linear filter applied is the “non-linear subtraction sliding minimum” filter. This filter computes the local minimum over a user defined scale pixel length. This filter was chosen to further increase the contrast, whereby local maxima of intensity are made visible. Due to the precious concentration filtering process, this second process results in a pure black-and-white image, with no gray. After the image processing was completed, the images were recompiled into a video clip using Blaze Media ProTM.

3.5 Laser lightsheet visualization

Laser lightsheet visualization was performed using PIV hardware and software. A schematic of the laser lightsheet system is given in Fig. 12. The imaging hardware is a LaVision FlowMaster 3D SPIV system that was installed on a custom-built mounting system. A cylindrical lens with a focal length of -10 mm spread a beam of light from a New Wave Research Solo 120 Nd:YAG double-pulsed laser into a 2.5 mm thick sheet. The figure

shows the lightsheet incident on the centerline of the flat plate, which also bisected one of the MVGs. An alternate arrangement had the lightsheet in a crosswise plane, 20.6 (0.81 in.) downstream of the MVG trailing edge.

The lasers were pulsed at 5 Hz with a pulse duration of $0.7 \mu\text{s}$. The images were captured by a Flow Master 3S ImagerIntense/ImagePro ICCD camera with 1376×1040 pixel resolution and a 12-bit dynamic range. Other major components of the imaging system included a frame grabber, control electronics and a host computer running the DaVis 7.1 PIV data acquisition and processing software.

A high-pressure seeding system was installed in the plenum chamber of the wind tunnel to spray calcium carbonate particles (Specialty Minerals CalEssence 70) with an average diameter of $0.7 \mu\text{m}$. It is thought that this is the first time that calcium carbonate has been used for such a purpose.

In addition to seeding the flow from the plenum chamber, local seeding was accomplished by naturally aspirating acetone from a 2.8 mm (0.11 in.) diameter surface pressure tap 138 mm (5.44 in.) upstream along the centerline of an MVG. A flexible tubing connected the pressure tap to a vial of acetone. Since the pressure in the test section was subatmospheric during a run, the acetone was drawn into the boundary layer via the tap. This local lightsheet visualization technique had been used previously in three-dimensional shock/boundary layer interaction studies.

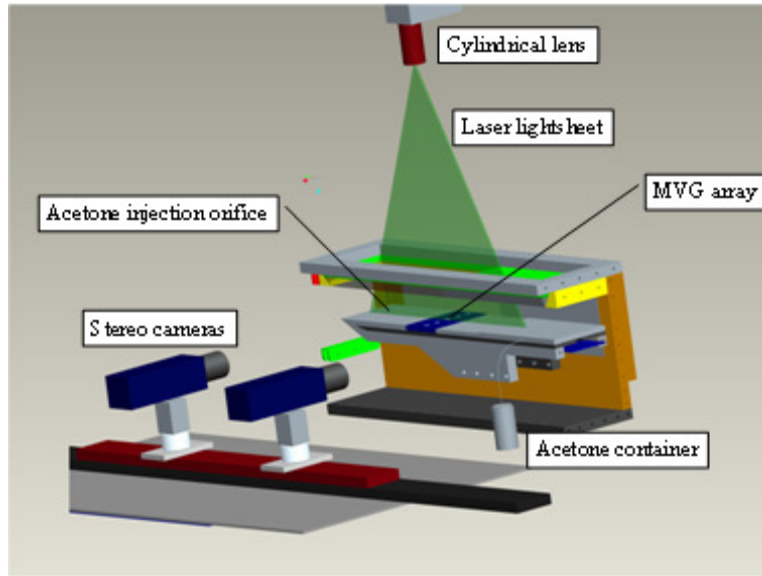


Figure 12. Schematic of laser lightsheet visualization hardware.

IV. New Discoveries

4.1 Discovery I: Spiral points and vortex structure around MVG

A pair of spiral points on the bottom plate and another pair on the sides of MVG (Fig. 13) have been found by ILES. These spiral points indicate the rising from the wall surface of the secondary vortex pairs. These new findings have been confirmed by UTA oil flow experiment (Fig. 14), which shows paint accumulation. A further comparison is given in Fig. 15.

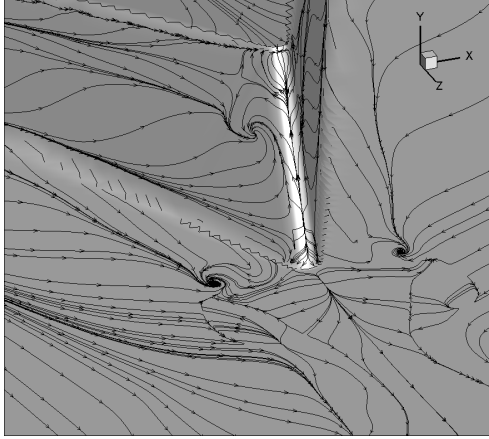


Figure 13. Spiral point pairs by ILES in 2009

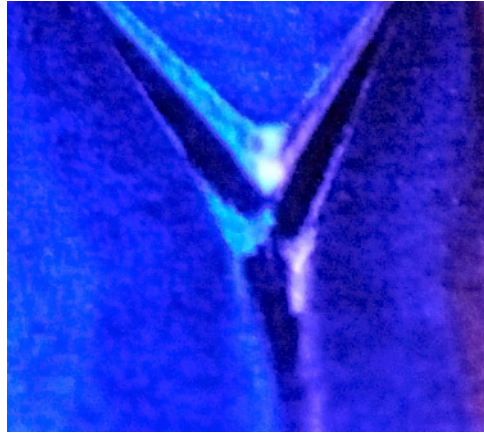


Figure 14. Oil accumulation blocks by UTA experiment in 2010

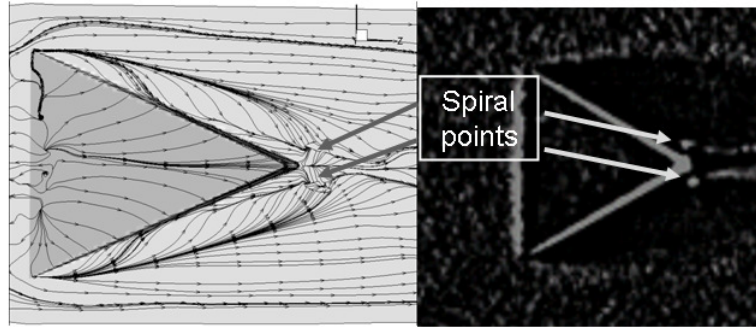


Figure 15. Comparison of ILES with UTA experiment

4.2 Discovery II: New model of five pairs of vortices near MVG

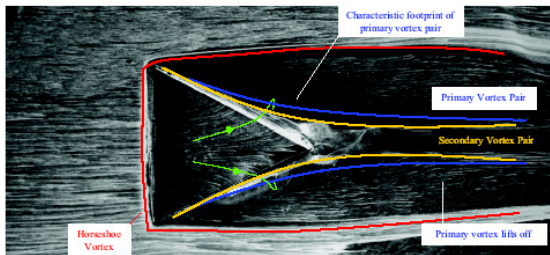


Figure 16. Traditional vortex structure around MVG

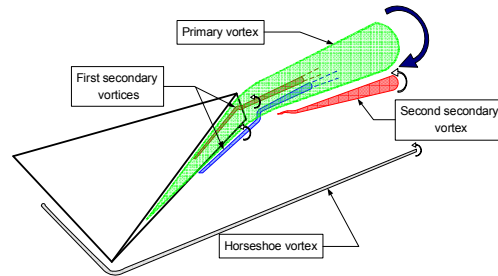


Figure 17. New 5-pair- vortex-tube model near MVG

The traditional vortex structure around MVG is depicted in Fig. 16 by Babinsky (2009), i.e., a pair of counter-rotating primary streamwise vortices is generated by MVG, which is mainly located within the boundary layer and which travel downstream for a considerable distance. Secondary vortices are located underneath the primary ones and even more streamwise vortices could be generated under suitable conditions. However, a new model of 5 pairs of vortex tubes near the MVG is given by us in Fig. 17. The main difference between the two models is that of the secondary vortex structures. There are two pairs of rising secondary vortex tubes corresponding to two pairs of spiral points. After the two pairs of secondary vortex tubes rising, a new pair of the secondary tubes is induced by the primary vortex tubes. Of course, there is additional one pair of horseshoe vortices. Recently in April 2010, the experimentalists in the University of Texas at Arlington (UT Arlington) took a video from the top view to record the process of the MVG oil flow. A distinct pair of oil accumulating points was found in the video (see the experimental snapshot in Figs. 14-15).

4.3 Discovery III : Surface separation topology

For comparison, the pictures of the surface oil flow from experiment and limiting streamlines from the computation are given in Figs 18-19. The topology of the two figures is essentially the same. The separation lines of the horseshoe vortex, the secondary separation lines beside the MVG and those after the MVG are clearly described by computation (Figs 20-21). Such lines are the most obvious traces found in experiment due to the deposit of the oil. Fig. 22 provides a comparison of computation and experiment in surface topology. The black area in experiment shows no oil flow from MVG top surface, which corresponds to flow separation in computation. The agreement

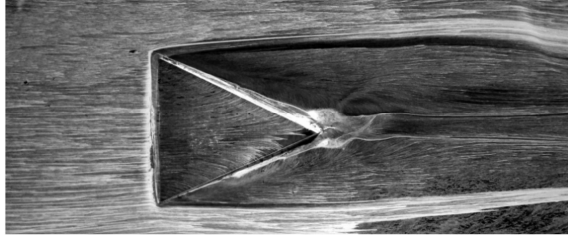


Figure 18. The surface oil flow by Babinsky7

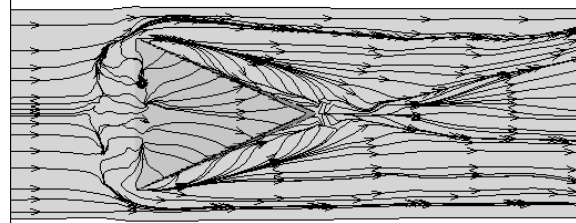


Figure 19. The surface limiting streamlines by computation

between computation and experiment is good.

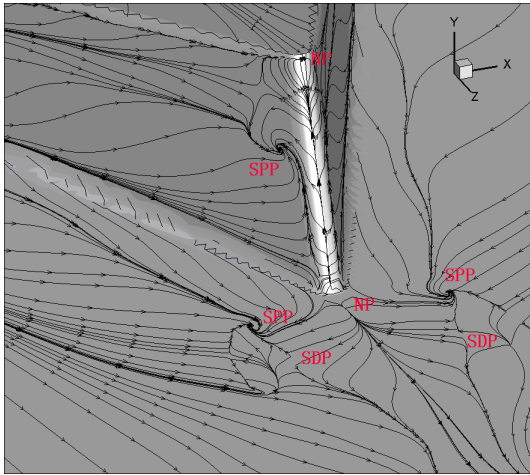
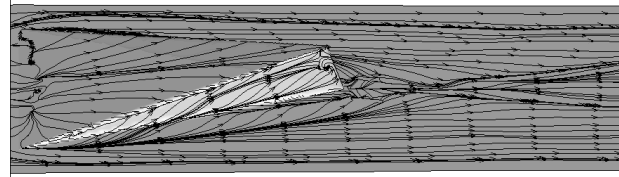
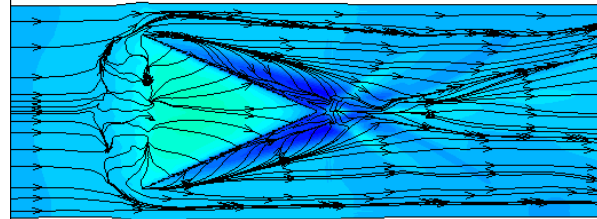


Figure 20. The separation pattern near the end of MVG

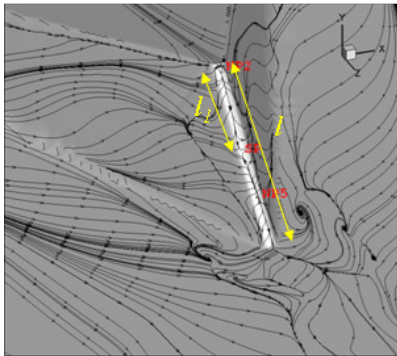


a) SSP on the side of MVG

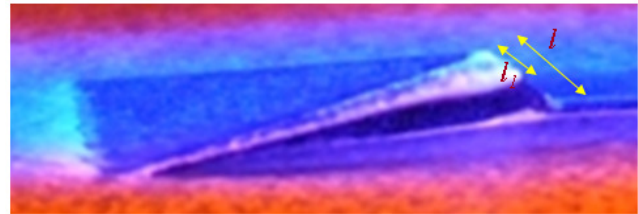


b) SSP backgrounded using the pressure contour

Figure 21. The various views of surface separation pattern (SSP)



a) Computation: $l_i/l=0.57$



b) Experiment: $l_i/l=0.545$

Figure 22. Comparison of ILES and experiment in surface flow topology

The original secondary vortex tubes induced by the primary vortex tubes on the bottom plate and MVG sides were lifted up from the spiral points and move further downstream around the primary (Figs 23-24). After that, a pair of new secondary vortex tubes is induced by the primary vortex tubes (Fig. 25).

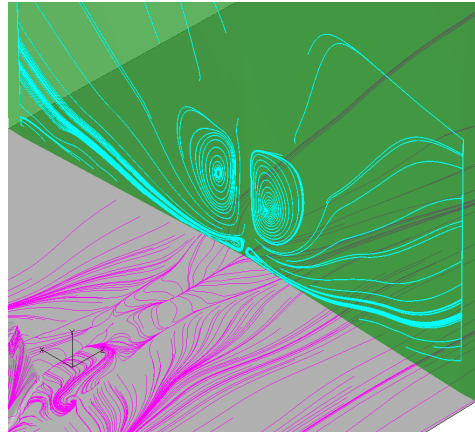
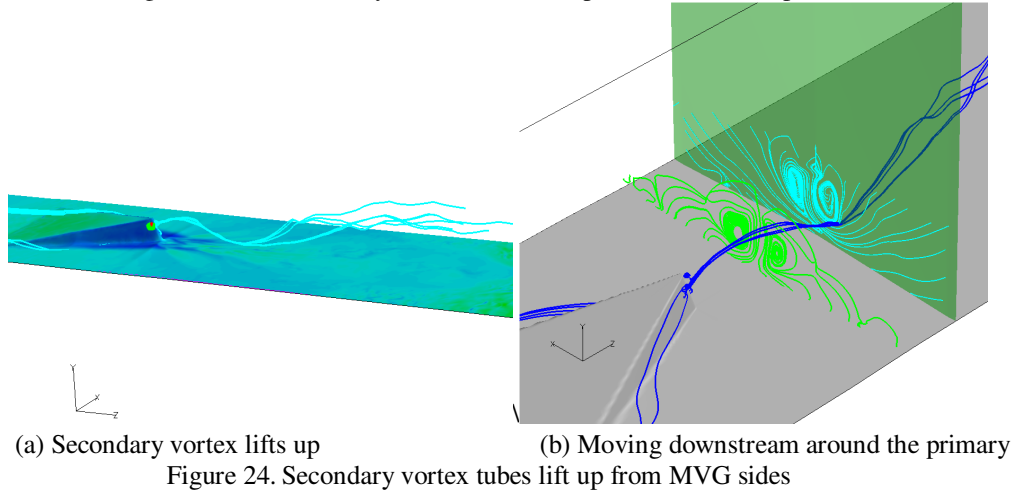
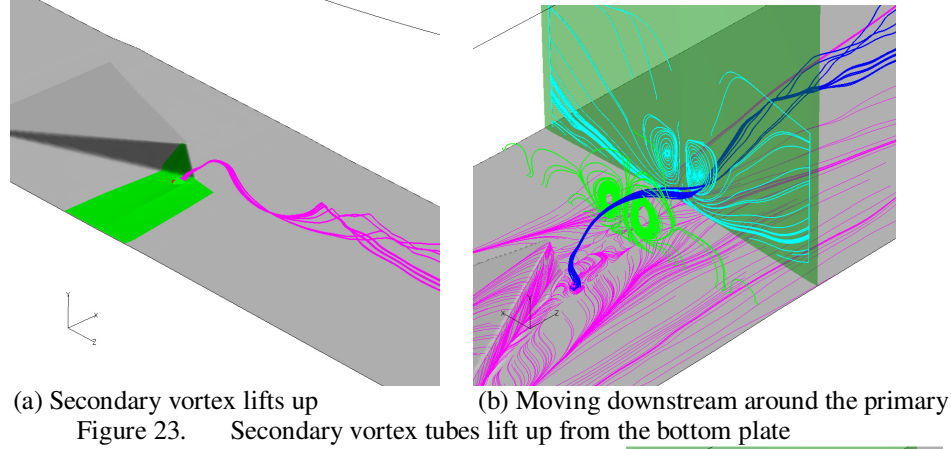


Figure 25. New secondary vortex tubes induced by the primary

4.4 Discovery IV: Origin of momentum deficit

The momentum deficit was first observed in the experiment by Babinsky (2007), and later confirmed by the computation of Ghosh, Choi and Edwards (2010) and Lee et al (2010), as shown in Fig. 26 using the averaged streamwise velocity at different sections. Babinsky thought that the momentum deficit region is the wake of MVG,

and Lee only mentioned “the two vortical tubes merge together to create a larger tube with two counter-rotating vortices inside”. What is the relation of the deficit to the flow structure? What does the low speed flow come from? The existing explanations did not provide a clear mechanism on the formation of the deficit.

In order to investigate the origins of the deficit, a heuristic analysis is made by investigating specific streamlines that are defined by certain cross-sections of the momentum deficit. First, a cross-section after the MVG is selected as a reference plane as shown in Fig. 27, and the momentum deficit on the plane is shown by using the contour of the instantaneous streamwise velocity, which appears in a green circular region. Next, we put some seeds around the boundary of the deficit and within the deficit area. Then we draw the 3-D streamlines starting from the seeds in both backward and forward directions. Because the seeds surround or locate within the deficit, the distribution of the backward streamlines qualitatively reflects the origins of the deficit. It can be seen from Fig. 22 that: a) all backward streamlines rotate around the primary streamwise vortex, which indicates that the formation of the deficit is caused by primary vortices; b) all backwards streamlines come from the upper surface of the MVG, which indicates that the main source of the deficit is the shedding of the upstream low-speed boundary layer, but is not the boundary layer flow around the MVG or after the MVG.

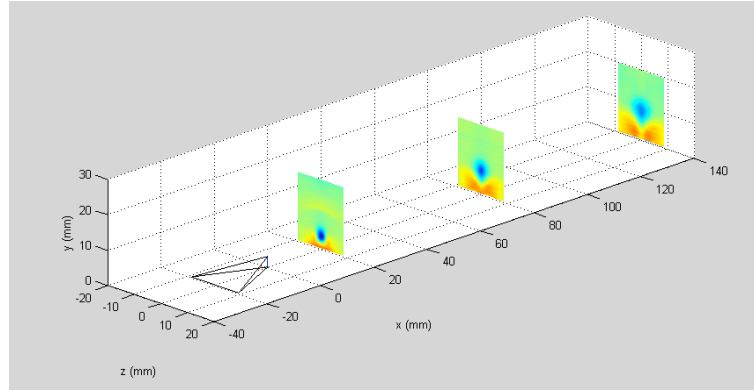
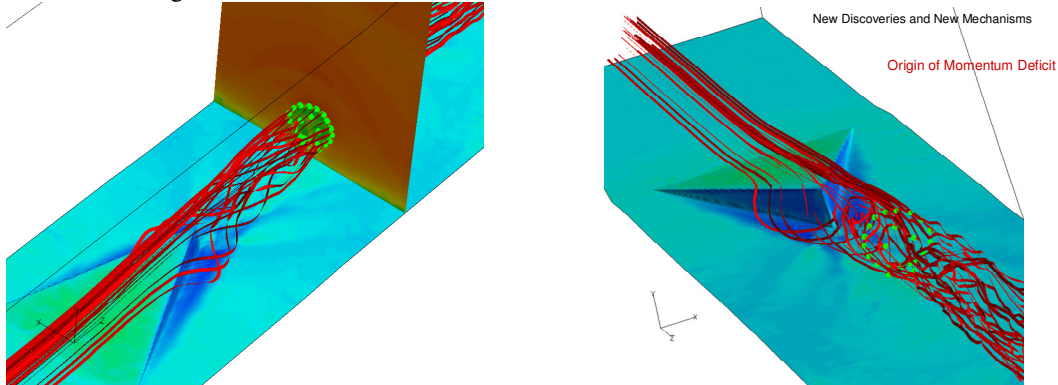


Figure 26. Momentum deficit shown in different streamwise directions



(a) Stream track for momentum deficit origin

(b) Locally enlarged stream tracks

Figure 27. Origin of the momentum deficit comes from the upper surface flow of MVG entrained by the primary vortex tubes

4.5 Discovery V: Inflection Surface, K-H instability and Vortex Ring Generation by MVG (Li et al 2010; Yan et al 2011)

4.5.1 2-D Kelvin-Helmholtz instability

Two-dimensional instability caused by shear layer with inflow disturbances and formation of pairing vortex rings were obtained by our previous calculation (Fig. 28). It is usually called Kelvin-Helmholtz instability which is described as an inviscid instability.

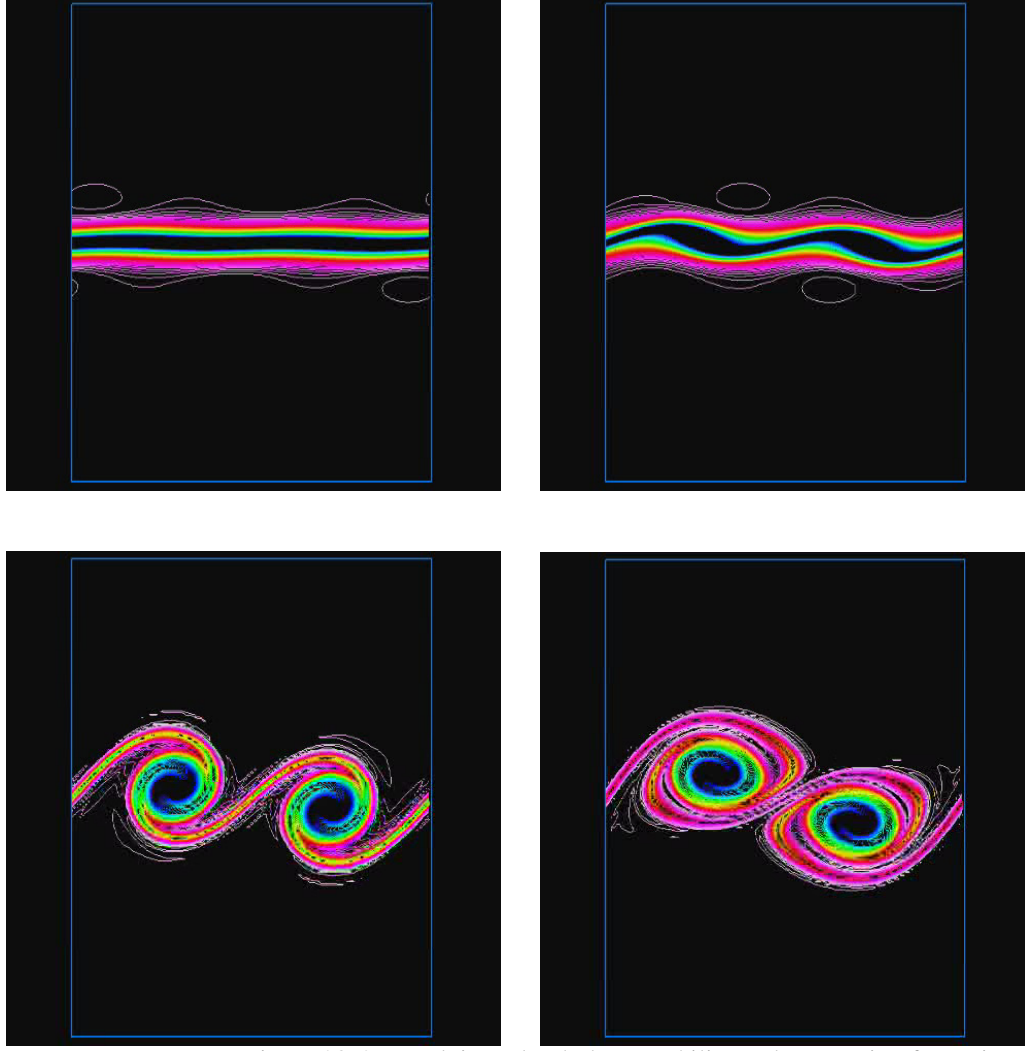


Figure 28. 2-D Kelvin-Helmholtz Instability and vortex ring formation

4.5.2 Inflection surface in 3-D flow behind MVG

In order to explore the mechanism of the vortex ring generation, the distributions of averaged streamwise-velocity are given in Fig. 24 along the normal grid lines at the center plane. The streamwise positions of the lines are $L_{from\ apex}/h \approx 3.3, 6.7, 10$ and 11 , where $L_{from\ apex}$ is the streamwise distance measured from the apex of MVG. The dip of the lines corresponds to the momentum deficit. From the results, it can be seen clearly that there are at least two high shear layers in the central plane, one is located at the upper edge of the dip and the other is located at the lower edge. Within the shear layer, there is at least one inflection point. In order to demonstrate the existence of the inflection points, the second order derivative $\partial^2 w / \partial y^2$ (w is the streamwise velocity and y is the normal direction) is calculated along the lines, and the result of the line at $L_{from\ apex}/h \approx 6.7$ is plotted in Fig. 25 as an example. The existence and correspondence of the inflection points at the upper and lower shear layers is illustrated by two dashed lines intersecting the distribution of the streamwise velocity and its second order derivative.

4.5.3 Vortex ring generation

Based on the above analyses, it can be concluded that the existence of the inflection points (surface in 3-D) in the shear layer causes the flow instability and generates vortex rollers by K-H instability in a cylindrical coordinate system. Therefore, the mechanism of the vortex ring generation should be K-H instability. The loss of the stability of the shear layer will result in the roll-up of the vortex, which appears in ring-like structure in a 3-D view (Fig. 26). In the Fig. 26(b), λ_2 is a certain eigenvalue of the stress tensor, and its iso-surface is usually used to describe the vortex surface. The intensity of the upper shear layer appears to be stronger than that of the lower shear layer (Fig. 31).

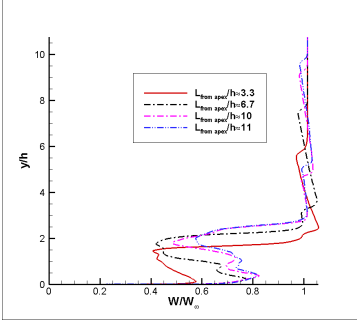
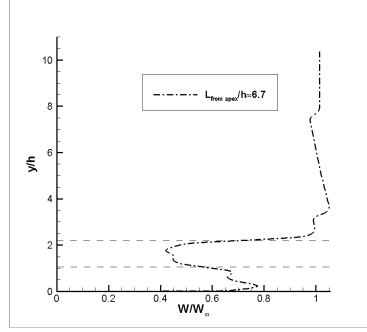


Figure 29. Averaged streamwise velocity at different sections



(a) Averaged streamwise velocity at $L_{\text{free apex}}/h \approx 6.7$

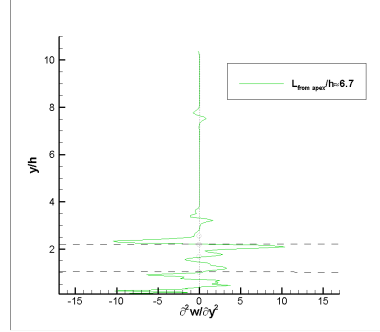
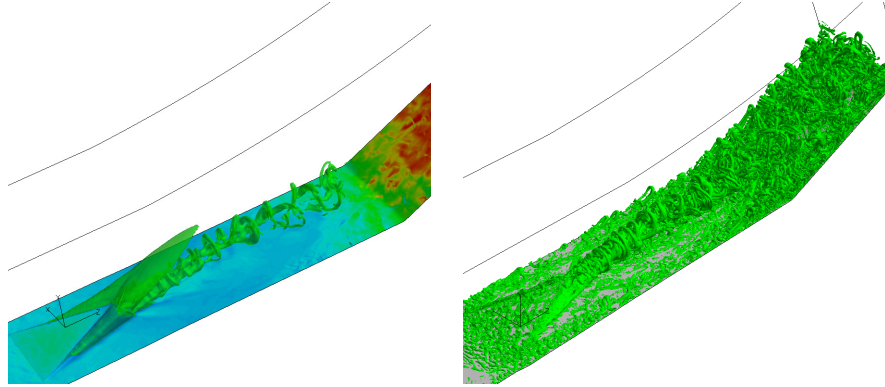


Figure 30. Inflection points (surface for 3-D)



(a) Iso-surface of pressure

(b) Iso-surface of λ_2

Figure 31. Vortex ring generation by MVG due to K-H instability

In Fig. 32, another qualitative checking of the shear layer and K-H instability is made by using the instantaneous flow field. In the figure, the background at the central plane and the spanwise plane is colored by the value of the streamwise velocity, so that the green regions in two planes represent the momentum deficit. In the central plane, the pressure contours are superimposed on the background cloud-map. The figure shows that, the blue circle structures, which indicate the core of the ring-like vortices cut by the plane are located on the boundary of the deficit circle. Such positions are exactly the same place where the high shear layer exists.

In Fig. 33, we give the instantaneous numerical schlieren picture at the central plane. From the figure, we can see numerous vortex rings appearing. After being told of the prediction of the vortex rings, the same experimentalists in UT Arlington tried novel visualization techniques to validate the discovery. They used vapor screen visualization and “panoramic” tracer visualization both in video and in micro-second flash photography. In Fig. 34, a typical image at the center plane is presented taken by using PIV and the acetone vapor (Lu et al, 2010). It is clearly demonstrated that a chain of vortex rings exist in the flow field after the MVG! And these structures qualitatively resemble that in Fig. 27-28.

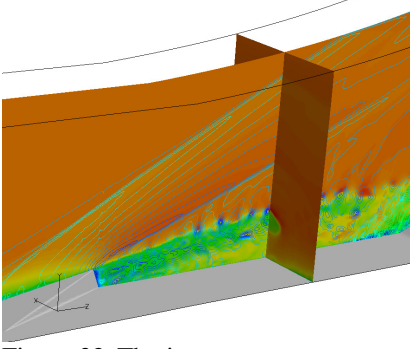


Figure 32. The instantaneous pressure and streamwise velocity contour on different cross sections

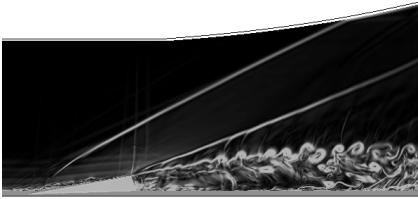
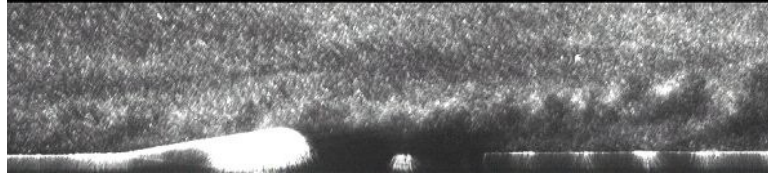
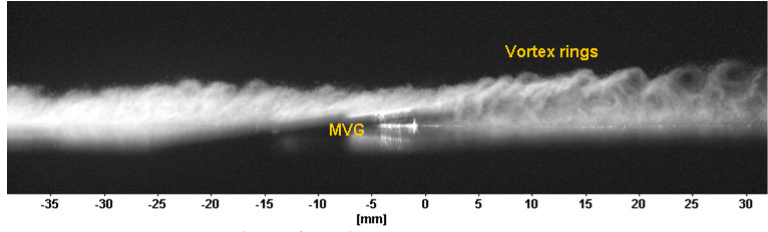


Figure 33. The numerical shilieren at the center plane



a) Using PIV



b) Using the acetone vapor

Figure 34. The laser-sheet flash image at the center plane

4.6 Discovery VI: Reduction of separation zone by ring-shock interaction

4.6.1 New mechanism of separation zone reduction by MVG

The traditional understanding of how an MVG works for flow control is that it produces streamwise vortices inside the boundary layer, which will bring low momentum fluid up from the bottom and high momentum fluid down to the boundary layer and then flow separation induced by a shock will be reduced due to the higher momentum. However, our LES just gives a quite different mechanism which can be described as follows. The MVG generates vortex rings and the vortex rings destroy the shocks thereby reducing the boundary layer separation bubble size.

Fig. 35 shows a graphic of the shock structure around a supersonic ramp, which includes a separation bubble shock and a reflection shock. The boundary layer separation is caused by the strong adverse pressure gradients induced by the shock. Many vortex rings are generated by the MVG and convect downstream toward the ramp. The rings first destroy the separation bubble shock as is evident in Fig. 36. The vortex rings are very stable and continue to move downstream to destroy the reflection shock as shown in Fig. 37. After many rings continuously move toward the reflection shock, the shock tail disappears and the separation area is substantially reduced (Fig. 38).

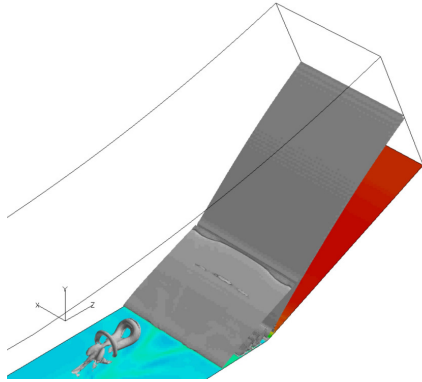


Figure 35. Shock structure around ramp

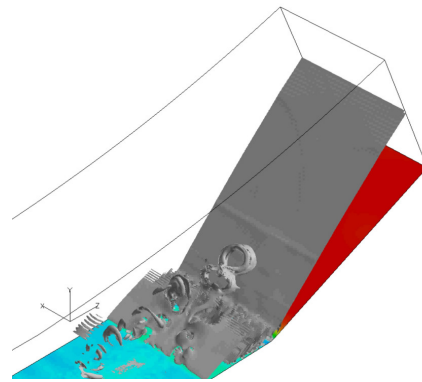


Figure 36. Ring-separation bubble shock interaction

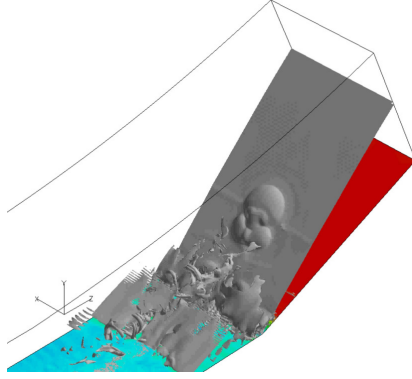


Figure 37. Ring-reflection shock interaction

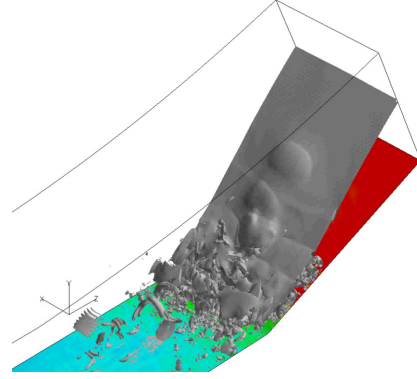


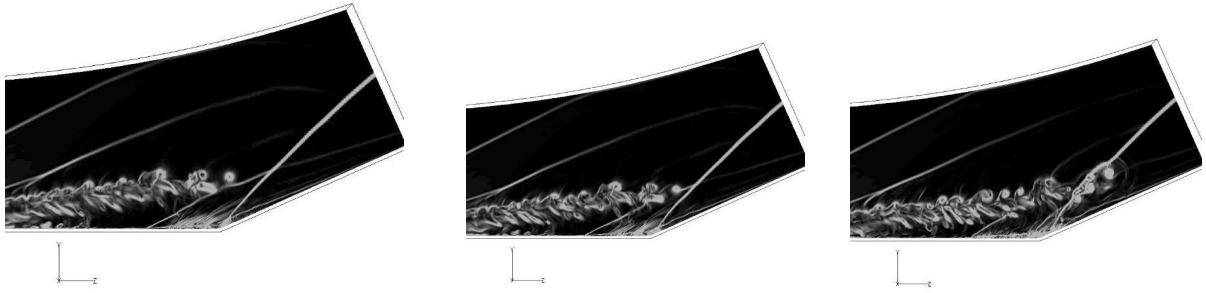
Figure 38. Separation reduction by vortex rings

4.6.2 Shock-vortex ring interaction

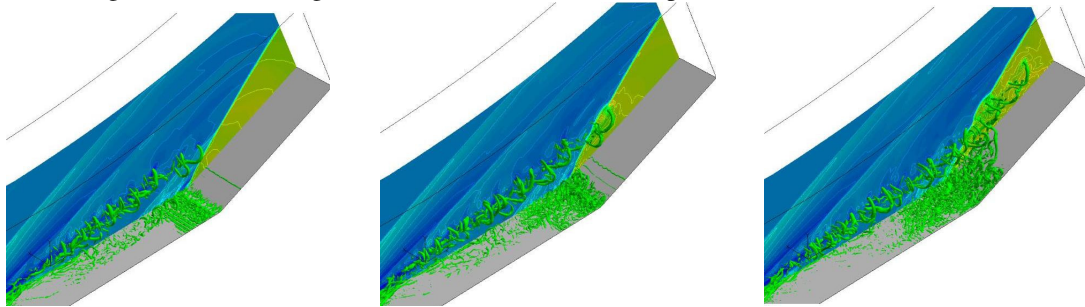
The mechanism as to why the vortex ring can destroy the shock is thought to arise from the low pressure inside the ring. On the other hand, the ring has a high pressure area at the rim and near the center which will change the shock location. The fast rotation of the ring could deform the shock surface.

4.6.3 Stable structure of the vortex ring

The shock is strong and the pressure gradients are large. We use both digital schlieren (Fig. 39) and λ_2 techniques (Fig. 40) for 3-D visualization and 2-D visualization on a central plane in the spanwise direction. The vortex rings are found to be very stable and keep their forms unchanged after passing the weak separation bubble shock and the strong ramp shock.



(a) Before the separation shock (b) Past the separation shock (c) Past the ramp shock
Figure 39. Vortex ring-shock interaction at the central plane (numerical schlieren)



(a) Before the shock (b) Hit the shock (c) Past the shock
Figure 40. Vortex ring-shock interaction at the central plane (λ_2 techniques)

4.7 Discovery VII: Three dimensional re-compressed shock structure

In Fig. 41, the spatial structures of the wave system are given by the instantaneous cross-section pressure contours. From the first section in Fig. 36a, the wave system is found to be the main reflection shock above the MVG and the expansion wave emanating from the edge of the MVG. The remaining sections show an arc-like structure of the re-compression shock wave, which is located behind the first reflection shock. The size of the arc keeps growing while moving downstream. The curved shape of the re-compression shocks implies that the function of the re-compression shock wave is to make the expansion flow satisfy the “virtual” boundary condition created by the streamwise vortices, at least at the initial stage of the formation of the shock wave. Detailed investigations show that, the head and feet of the arc-like shock are separated from each other in the initial stage (see Fig. 41(b)). They begin to connect and form a complete arc at a certain downstream location, as shown in Fig. 41(c).

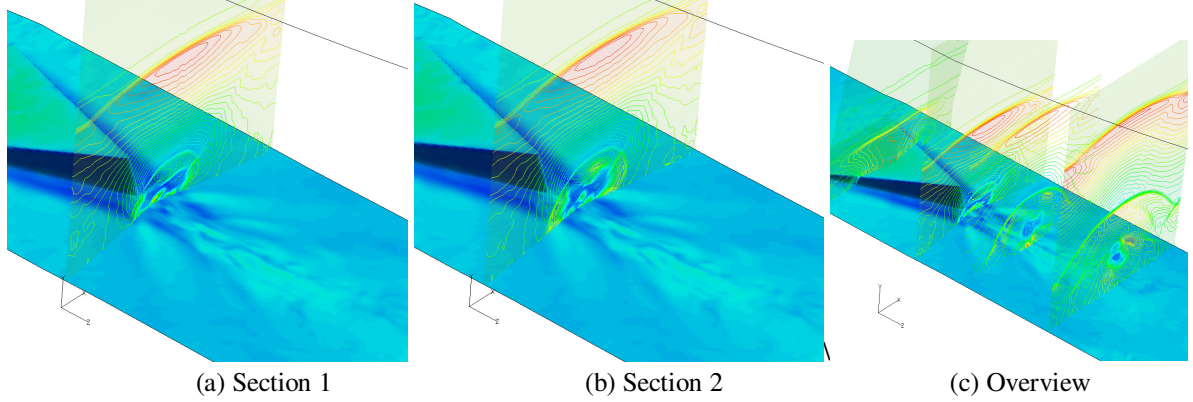


Figure 41. The 3-D structure of the re-compression shock

4.8 Discovery VIII: Effects of trailing-edge decline angles

Comparative studies are made on the MVG flow at $M=2.5$ and $Re_\theta=1440$ while the MVGs are of different trailing edge angle, i.e., $\beta=70^\circ$ and $\beta=45^\circ$. The numerical study finds (see Fig. 42):

- 1) The basic structures are similar in two cases, like the wave system, separation pattern, momentum deficit and the vortex rings, etc. The effect of declining angle does not bring about the structural difference, while differences exist in the details of the flow.
- 2) The smaller declining angle at $\beta=45^\circ$ makes the vortices closer to the wall, which include the initial streamwise vortices and the layer vortex rings. This should be more favorable to flow control. Nevertheless, the quantitative analyses on the time-averaged data at a downstream do not exhibit a significant improvement about the quality of the boundary layer.

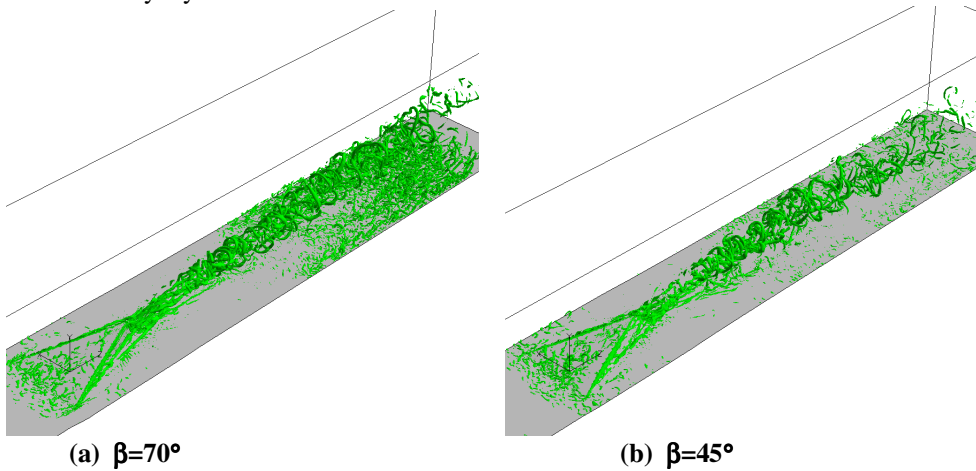


Figure 42. Comparison of the vortex structure with different decline angles of MVG trailing edge

IV Conclusions

The following new discoveries and new mechanisms have been made by implicit LES since 2009. Most of these new findings were confirmed later by UTA experiment in 2010:

- 1) Detailed flow structures (topology) around MVG and spiral points are found. Then the new five pairs of vortex tubes model around MVG is given.
- 2) Origin of the momentum deficit is found - not only caused by stream wise vortices through mushroom, but also, mainly, viscosity of MVG and wall surface.
- 3) Inflection points (surface in 3-D) inside the deficit area are found.
- 4) Kelvin-Helmholtz type instability is caused by the momentum deficit.
- 5) Vortex rings are generated by K-H type instability after MVG.
- 6) Shock-ring interaction is found.
- 7) Mechanism of MVG for separation reduction is due to the ring shock interaction, not only mixing as traditional explanation on VG or MVG.
- 8) Ring is the only form of vortex inside the fluid field and never breaks down.
- 9) Structure of re-compressed shock is found.
- 10) Influence of the MVG trailing edge decline angles is studied.

All these new findings may be very important to regular VG, subsonic flow, flow control, flow transition and turbulence studies.

Acknowledgments

This work is supported by AFOSR grant FA9550-08-1-0201 monitored by Dr. John Schmisser. The authors are grateful to the Texas Advanced Computing Center (TACC) for providing computation hours.

References

- [1] Anderson, B.H., Tinapple J., and Surber, L., "Optimal Control of Shock Wave Turbulent Boundary Layer Interaction Using Micro-Array Actuation," *AIAA paper 2006-3197*.
- [2] Ashill, P.R., Fulker, J.L., and Hackett, K.C., "A Review of Recent Developments in Flow Control," *The Aeronautical Journal*, 109, 1095, 2005, pp.205-232.
- [3] Babinsky, H., Li, Y., and Ford, C.W.P., "Microramp Control of Supersonic Oblique Shock-Wave/Boundary-Layer Interactions," *AIAA J.*, Vol. 47, No. 3, 2009, pp.668-675.
- [4] Ford, C.W.P. and Babinsky, H., "Micro-Ramp Control for Oblique Shock Wave/Boundary Layer Interaction," *AIAA paper 2007-4115*.
- [5] Ghosh, S., Choi, J., and Edwards, J.R., "Numerical Simulations of the Effects of Micro Vortex Generators Using Immersed Boundary Methods," *AIAA JOURNAL*, Vol. 48, No. 1, January 2010
- [6] Holden, H.A. and Babinsky, H., "Vortex Generators Near Shock/Boundary Layer Interactions," *AIAA paper 2004-1242*.
- [7] Holden, H.A. and Babinsky, H., "Effect of Microvortex Generators on Separated Normal Shock/Boundary Layer Interactions," *AIAA J.*, 2007, pp.170-173.
- [8] Jiang, G., and Shu, C.W., "Efficient Implementation of Weighted ENO Schemes," *J. Comput. Phys.*, Vol. 126, 1996, pp.202-228.
- [9] Lee, S. and Loth, E., "Supersonic Boundary Layer Interactions with Various Micro-Vortex Generator Geometries," *AIAA Paper 2009-3712*.
- [10] Lee, S. and Loth E., "Microramps Upstream of an Oblique-Shock/Boundary-Layer Interaction," *AIAA JOURNAL*, Vol. 48, No. 1, January 2010
- [11] Li, Q. and Liu, C., "LES for Supersonic Ramp Control Flow Using MVG at $M=2.5$ and $Re_\theta=1440$ ", *AIAA* 2010-592
- [12] Li, Q. and Liu, C., "Numerical Investigations on the Effects of the Declining Angle of the Trailing-Edge of MVG", *AIAA Journal of Aircraft*, Vol 47, No. 6, pp2086-2095, 2011,
- [13] Li, Q., Yan, Y., Liu C., Lu, F., and Pierce, A., "Numerical and experimental studies on the separation topology of the MVG controlled flow at $M=2.5$ and $Re_\theta=1440$," *AIAA-2011-0072*, the 49th AIAA Aerospace Sciences Meeting, Florida, 2011.

- [14] Li, Q., Yan, Y., and Liu C., "The interaction between vortex rings and the oblique shock by the MVG controlled ramp flow at $M=2.5$ and $Re_\theta=1440$," AIAA-2011-0861, the 49th AIAA Aerospace Sciences Meeting, Florida, 2011.
- [15] Lin, J.C. "Review of Research on Low-Profile Vortex Generators to Control Boundary-Layer Separation," *Progress in Aerospace Sciences*, Vol. 38, 2002, pp.389-420.
- [16] Liu, C. and Chen, L., "Study of Mechanism of Ring-Like Vortex Formation in Late Flow Transition," *AIAA Paper 2010-1456*.
- [17] Loginov, M.S., Adams, N.A. and A. A. Zheltovodov, A.A., "Large-Eddy Eimulation of Shock-Wave/Turbulent-Boundary-Layer Interaction," *J. Fluid Mech.*, Vol. 565, 2006, pp. 135-169.
- [18] Lu, F., Pierce, A. and Shih, Y., "Experimental study of near wake of micro vortex generators in supersonic flow, " *AIAA paper 2010-4623*.
- [19] Yan, Y., Li, Q., Liu, C., and Lu, F., Numerical and Experimental Studies on Mechanism of K-H Instability and Ring Generation behind Supersonic MVG, AIAA Paper 2011-0676/49th AIAA Aerospace Sciences Meeting, AIAA-2011-0676,

Attachment:

List of publications supported or partially supported by this grant:

I Journal Papers (Published or Accepted):

1. Numerical Investigations on the Effects of the Declining Angle of the Trailing-Edge of MVG, AIAA Journal of Aircraft, Vol 47, No. 6, pp2086-2095, 2011, Qin Li & Chaoqun Liu
2. Numerical Study on Mechanisms of Second Sweep and Positive Spikes in Transitional Flow on a Flat Plate, Journal of Computers and Fluids, Vol 40, pp28-41, 2011, Lin Chen & Chaoqun Liu
3. New Shock Detector for Shock-Boundary Layer Interaction, High Performance Computing and Applications, Springer , ISSN 0302-9743, pp78-87, March 2010, Maria Oliveira & Chaoqun Liu
4. Late-Stage Vortical Structures and Eddy Motions in a Transitional Boundary Layer, CHIN. PHYS. LETT. Vol. 27, No. 2 (2010) 024706, Xiaobing Liu, Zhengqing Chen, Chaoqun Liu.
5. Evolution in the ring-like vortices and spike structure in transitional boundary, Science of China, Physics, Mechanics & Astronomy, Vol.53 No.3: pp514-520, March, 2010, Lin Chen, Xiaobing Liu, Dengbing Tang, Maria Oliveira and Chaoqun Liu.
6. New Shock/Discontinuity Detector, International Journal of Computer Mathematics, July 29, 2010, Maria Oliveira, Ping Lu, Xiaobing Liu, Chaoqun Liu
7. High Order Compact Scheme for Boundary Points, International Journal of Computer Mathematics, Volume 87, Issue 8 July 2010 , pages 1795 – 1819, Ping Lu, Maria Oliveira and Chaoqun Liu
8. Truncation Error, Dissipation and Dispersion Terms of 5th Order WENO and of WCS for 1D Conservation Law, International Journal of Computer Mathematics, Volume 887, Issue 2 February 2010, pages 339 - 352, Maria Oliveira, Jianzhong Su, Peng Xie, Chaoqun Liu
9. Parallel DNS for Vortex Structure of Late Stages of Flow Transition, Journal of Computers and Fluids, Special Issue for PARCFD2001, to appear, Chaoqun Liu and Lin Chen
10. Modified Upwinding Compact Scheme for Shock and Shock Boundary Layer Interaction, CiCP (Communication in Computational Physics), to appear, Chaoqun Liu, Ping Lu and Maria Oliveira
11. Numerical and Theoretical Study on "Vortex Breakdown", International Journal of Computer Mathematics, to appear, Chaoqun Liu
12. Implicit LES for Supersonic Microramp Vortex Generator - New Discoveries and New Mechanisms, Advances in Computational Fluid Dynamics and Its Applications, Special Issue of Journal of Modeling and Simulation in Engineering, to appear, Qin Li and Chaoqun Liu
13. New Findings by High Order DNS for Late Flow Transition in a Boundary Layer, Advances in Computational Fluid Dynamics and Its Applications, Special Issue of Journal of Modeling and Simulation in Engineering, to appear, Chaoqun Liu, Lin Chen, Ping Lu
14. Evolution of the vortex structures and turbulent spots at the late-stage of transitional boundary layers, Science China Ser G, to Appear, Lin Chen, Denbing Tang, Ping Lu, Chaoqun Liu

II AIAA Papers (Published):

1. Improvement of Mixing Function for Modified Upwinding Compact Scheme, AIAA Paper 2011-0368/49th AIAA Aerospace Sciences Meeting, AIAA- January 2011, H. Fu, P. Lu and C. Liu
2. Numerical Study of Mechanism of U-Shaped Vortex Formation, AIAA Paper 2011-0286/49th AIAA Aerospace Sciences Meeting, AIAA- January 2011, Ping Lu and Chaoqun Liu
3. Numerical Study of Mechanism of Small Vortex Generation in Boundary Layer Transition, AIAA Paper 2011-0287/49th AIAA Aerospace Sciences Meeting, AIAA- January 2011, Ping Lu and Chaoqun Liu
4. Numerical and Experimental Studies on Mechanism of K-H Instability and Ring Generation behind Supersonic MVG, AIAA Paper 2011-0676/49th AIAA Aerospace Sciences Meeting, AIAA- January 2011, Yonghua Yan, Qin Li, Chaoqun Liu and Frank Lu
5. Numerical and experimental studies on the separation topology of the MVG controlled flow at $M=2.5$ and $Re=1440$, AIAA2011-0072/49th AIAA Aerospace Sciences Meeting, Q. Li, Y. Yan, F. Lu, A. Pierce and C. Liu
6. The interaction between vortex rings and the oblique shock by the MVG controlled ramp flow at $M=2.5$ and $Re=1440$, AIAA2011-0861/49th AIAA Aerospace Sciences Meeting, Q. Li, Y. Yan and C. Liu
7. Review of Micro Vortex Generators in High-Speed Flow, AIAA Paper 2011-0031/49th AIAA Aerospace Sciences Meeting, F. Lu, A. Pierce, Y. Shih, Q. Li, C. Liu
8. Interaction of Microvortex Generator Flow with Ramp-Induced Shock/Boundary-Layer Interactions, AIAA-ASM 2011/49th AIAA Aerospace Sciences Meeting, AIAA Paper 2011-0032, F. Lu, A. Pierce, Y. Shih, Q. Li, C. Liu
9. Experimental and Numerical Study of Flow Topology Past Micro Vortex Generators, AIAA-2010-4463, June 2010, F. Lu, A. Pierce, Y. Shih, Q. Li, C. Liu
10. LES for Supersonic Ramp Flow Control Using MVG at $M=3$ and $Re=2400$ AIAA Paper Number 2010-592, Qin Li and Chaoqun Liu, January 2010
11. Numerical Investigations on the Effects of the Declining Back-Edge of MVG AIAA Paper Number 2010-714, with Qin Li, January 2010
12. Implicit LES for Shock/Blunt Body Interaction AIAA Paper Number 2010-874, Maria Oliveira and Chaoqun Liu, January 2010
13. Modified Weighted Compact Scheme for 1-D and 2-D Shock / Wave Interaction AIAA Paper Number 2010-723, Maria Oliveira and Chaoqun Liu, January 2010
14. DNS for Late Stage Structure of Flow Transition on a Flat-Plate Boundary Layer AIAA Paper Number 2010-1470, Xiaobing Liu, Lin Chen, Maria Oliveira, Dengbing Tang and Chaoqun Liu, January 2010
15. DNS for Ring - Like Vortices Formation and Roles in Positive Spikes Formation AIAA Paper Number 2010-1471, Lin Chen, Xiaobing Liu, Maria Oliveira and Chaoqun Liu, 2010
16. Study of Mechanism of Ring-Like Vortex Formation in Late Flow Transition AIAA Paper Number 2010-1456, Chaoqun Liu and Lin Chen, January 2010
17. Universal High Order Subroutine with New Shock Detector for Shock Boundary Layer Interaction, AIAA-2009-1139, M. Oliveria, P. Lu, X. Liu and C. Liu
18. Laser alignment method for portable schlieren system, 39th AIAA Fluid Dynamics Conference, AIAA 2009-3574, 22-25 June 2009, San Antonio, Texas, A.J. Pierce and F.K. Lu